



University of Glasgow  
DEPARTMENT OF

**AEROSPACE  
ENGINEERING**



**Implementation and Validation of  
the Spalart-Allmaras Turbulence  
Model in the PMB3D Code**

**Aerospace Engineering Report 0213**

**Xiaobo Yang**

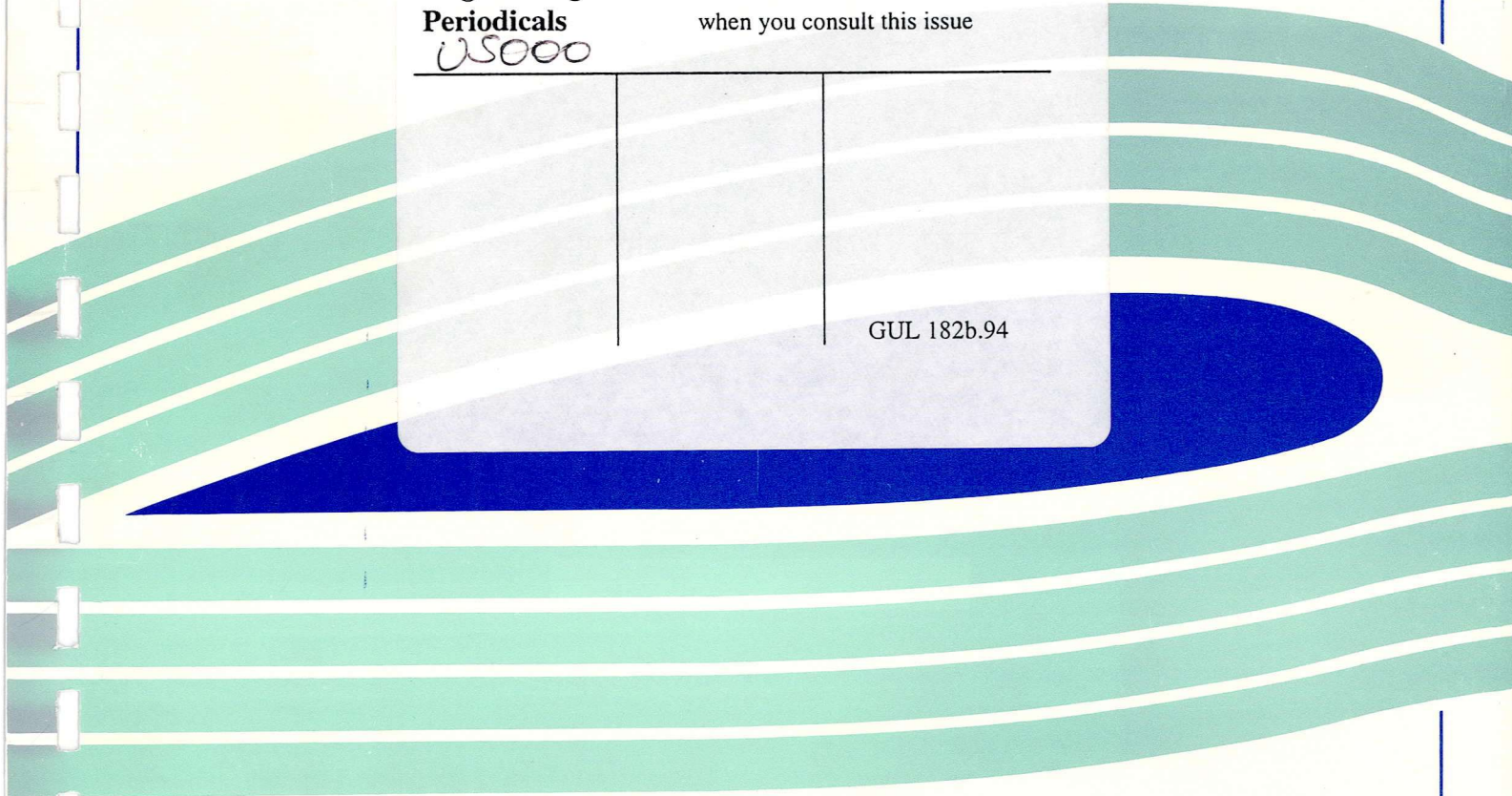
**Engineering  
Periodicals**

U5000

Please initial and date below  
when you consult this issue

--	--	--

GUL 182b.94



Implementation and Validation of  
the Spalart-Allmaras Turbulence  
Model in the PMB3D Code

Aerospace Engineering Report 0213

Xiaobo Yang

Department of Aerospace Engineering  
University of Glasgow  
Glasgow G12 8QQ  
United Kingdom

November 2002

## Abstract

The Spalart-Allmaras one-equation turbulence model has been implemented and validated in the PMB3D code, which is a parallel multi-block computational fluid dynamics (CFD) code developed at the University of Glasgow. Different test cases including turbulent flows around RAE2822 Cases 9 and 10, NLR-F5 wing, ONERA A aerofoil, AGARD Case CT2 and 18% circular arc aerofoil have been performed. In general when compared with the experimental data, the performance of the S-A model is good. For some test cases, results of this model are also compared with the  $k-\omega$  two-equation turbulence model. It has been observed that the S-A model is similar to the two-equation  $k-\omega$  model in attached flows.

## Contents

List of Tables	3
List of Figures	4
Nomenclature	7
<b>1 Introduction</b>	<b>1</b>
<b>2 Implementation</b>	<b>1</b>
2.1 S-A turbulence model transport equation . . . . .	1
2.2 Non-dimensionalisation . . . . .	3
2.3 Curvilinear coordinates . . . . .	5
2.4 Finite volume method . . . . .	7
2.5 Spatial discretisation . . . . .	8
2.5.1 Inviscid flux terms . . . . .	9
2.5.2 Viscous flux terms . . . . .	10
2.5.3 Source term . . . . .	11
2.6 Boundary conditions . . . . .	11
2.7 Time discretisation . . . . .	12
2.7.1 Steady-state solver . . . . .	12
2.7.2 Unsteady flow solver . . . . .	13
2.8 Linear solver . . . . .	14
<b>3 Validation</b>	<b>15</b>
3.1 RAE2822 aerofoil Cases 9 and 10 . . . . .	15
3.2 NLR-F5 wing . . . . .	17
3.3 ONERA A aerofoil . . . . .	19
3.4 AGARD Case CT2 . . . . .	21
3.5 Self excited test case . . . . .	23

4 Conclusions

26

References

27

## List of Tables

1	Boundary conditions for the S-A turbulence model . . . . .	12
2	Flow conditions selected for the RAE2822 Cases 9 and 10 . . . . .	15

## List of Figures

2.1	<i>Coordinate transformation from physical to computational domain . . .</i>	5
2.2	<i>Two types of finite volume grids: (a) nodes centered in CVs (b) CV faces centred between nodes . . . . .</i>	8
2.3	<i>Approximate Jacobian matrix . . . . .</i>	13
3.1	<i>Mach number contours around the RAE2822 aerofoil . . . . .</i>	15
3.2	<i>Pressure coefficient distributions for the RAE2822 aerofoil . . . . .</i>	16
3.3	<i>Skin friction coefficient distributions for the RAE2822 aerofoil . . . . .</i>	16
3.4	<i>Pressure contours for NLR-F5 wing . . . . .</i>	17
3.5	<i>Pressure coefficient distribution for NLR-F5 Wing . . . . .</i>	18
3.6	<i>Pressure coefficient distribution along the ONERA A aerofoil . . . . .</i>	19
3.7	<i>Velocity profiles along the ONERA A aerofoil . . . . .</i>	20
3.8	<i>Integrated normal force for NACA0012 aerofoil case CT2 . . . . .</i>	22
3.9	<i>Instantaneous pressure distributions for NACA0012 aerofoil case CT2 .</i>	22
3.10	<i>Normal force coefficient history for 18% circular arc aerofoil test case .</i>	23
3.11	<i>Steady pressure and skin friction distributions for 18% circular arc aero- foil test case CT2 . . . . .</i>	24
3.12	<i>Unsteady pressure and skin friction distribution sequence for 18% circu- lar arc aerofoil test case, <math>M_\infty = 0.77</math>, <math>Re = 2 \times 10^6</math> . . . . .</i>	25

## Nomenclature

$c$	chord length
$C_p$	pressure coefficient, $C_p = (p - p_\infty)/(\frac{1}{2}\rho_\infty U_\infty^2)$
$C_f$	skin friction, $C_f = \tau_w/(\frac{1}{2}\rho_\infty U_\infty^2)$
$F, G, H$	functions/fluxes
$\mathbf{F}, \mathbf{G}$ ,	convective fluxes
$\mathbf{I}$	identity matrix
$\mathbf{J}$	Jacobian matrix
$k$	kinetic energy of turbulent fluctuations, $k = \frac{1}{2}\overline{u'_i u'_i} = \frac{1}{2}(\overline{u'^2} + \overline{v'^2} + \overline{w'^2})$
$M$	Mach number
$p$	pressure
$Pr$	Prandtl number, $Pr = \mu c_p/k = 0.72$
$Pr_t$	turbulent Prandtl number, $Pr_t = \mu_t c_p/k = 0.90$
$\mathbf{Q}$	vector of conservative variables
$\mathbf{R}$	residual vector
$Re$	Reynolds number
$S$	source term
$S_{ij}$	mean strain rate tensor, $S_{ij} = \frac{1}{2}(\frac{\partial u_i}{\partial x_j} + \frac{\partial u_j}{\partial x_i})$
$t$	time
$u, v$	velocity components
$u_\tau$	friction velocity, $u_\tau = \sqrt{\tau_w/\rho_w}$
$\overline{u'_i}, \overline{u'_j}$	temporal average of fluctuating velocities
$V$	control volume
$x, y$	cartesian coordinates
$y^+$	dimensionless wall distance, $y^+ = u_\tau y/\nu$

### Greek Symbols

$\alpha$	angle of attack
$\eta$	position along spanwise direction
$\kappa$	von Karman constant, $\kappa = 0.41$
$\mu$	laminar molecular viscosity
$\mu_t$	turbulent eddy viscosity
$\nu$	kinematic molecular viscosity, $\nu = \mu/\rho$
$\nu_t$	kinematic eddy viscosity, $\nu_t = \mu_t/\rho$
$\tilde{\nu}$	undamped eddy viscosity in the S-A turbulence model
$\xi, \eta, \zeta$	curvilinear coordinates
$\rho$	density
$\sigma$	closure coefficient of turbulence model
$\tau$	stress
$\chi$	working variable, $= \tilde{\nu}/\nu$
$\omega$	specific turbulent dissipation rate, $\omega = \epsilon/k$
$\Omega$	absolute value of vorticity

### Superscripts

$i$	inviscid
$v$	viscous
*	non-dimensionalised value

### Subscripts

$i, j, k$	location of control volume
$w$	wall values
$x, y$	components in x, y directions

$\infty$  freestream values

## 1 Introduction

Turbulence model plays an important role in computational fluid dynamics (CFD). In the past fifty years, many turbulence models have been developed. The most commonly used turbulence models today are eddy viscosity models including zero-, one- and two-equation models. The Spalart-Allmaras turbulence model is a one-equation eddy viscosity model [1, 2]. It was inspired from an earlier model developed by Baldwin and Barth [3]. The transport equation and coefficients of the S-A model were defined using dimensional analysis, Galilean invariance, and selected empirical results.

The S-A model has been implemented and validated by many researchers in the past ten years [4, 5, 6, 7, 8, 9, 10, 11]. The model was highly recommended [4, 5] for attached flows. It can give results that are often similar to the two-equation models, particularly to the Menter's *SST* model. However it performs less well in separated flows. In this report, implementation and validation of the S-A model into the PMB3D code is presented. The PMB3D code is a generic CFD code developed at the University of Glasgow.

## 2 Implementation

### 2.1 S-A turbulence model transport equation

As described in the previous section, the S-A turbulence model is a one-equation model developed by Spalart and Allmaras [1, 2]. The transport equation and coefficients of the S-A model were defined using dimensional analysis, Galilean invariance, and selected empirical results. The original S-A model has transition modifiers built in to trip the boundary layer to transition. Here all these modifiers are ignored, so all the calculations are run fully turbulent. The Reynolds stresses are given by

$$-\overline{u'_i u'_j} = 2\nu_t S_{ij}, \quad (1)$$

where  $S_{ij}$  is the mean strain rate tensor. The eddy viscosity  $\nu_t$  is given by

$$\nu_t = \tilde{\nu} f_{v1}, \quad f_{v1} = \frac{\chi^3}{\chi^3 + c_{v1}^3}, \quad \chi \equiv \frac{\tilde{\nu}}{\nu}. \quad (2)$$

$\nu$  is the molecular viscosity.  $\tilde{\nu}$  is the working variable and obeys the following transport equation

$$\begin{aligned} \frac{D\tilde{\nu}}{Dt} = & c_{b1} [1 - f_{t2}] \tilde{\Omega} \tilde{\nu} + \frac{1}{\sigma} [\nabla \cdot ((\nu + \tilde{\nu}) \nabla \tilde{\nu}) + c_{b2} (\nabla \tilde{\nu})^2] \\ & - \left[ c_{w1} f_w - \frac{c_{b1}}{\kappa^2} f_{t2} \right] \left[ \frac{\tilde{\nu}}{d} \right]^2 + f_{t1} \Delta U^2. \end{aligned} \quad (3)$$

The left hand side of the equation is the Lagrangian or material derivative of  $\tilde{\nu}$ :  $D\tilde{\nu}/Dt \equiv \partial\tilde{\nu}/\partial t + u_i \partial\tilde{\nu}/\partial x_i$ ,  $\tilde{\Omega}$  is the modified magnitude of the vorticity and  $d$  is the distance to the closest wall. Here

$$\tilde{\Omega} \equiv \Omega + \frac{\tilde{\nu}}{\kappa^2 d^2} f_{v2}, \quad f_{v2} = 1 - \frac{\chi}{1 + \chi f_{v1}}. \quad (4)$$

The other auxiliary functions are defined by

$$\begin{aligned} f_w = g \left[ \frac{1 + c_{w3}^6}{g^6 + c_{w3}^6} \right]^{1/6}, \quad g = r + c_{w2} (r^6 - r), \quad r \equiv \frac{\tilde{\nu}}{\tilde{S} \kappa^2 d^2}, \\ f_{t2} = c_{t3} \exp(-c_{t4} \chi^2), \quad f_{t1} = c_{t1} g_t \exp \left( -c_{t2} \frac{\omega_t^2}{\Delta U^2} [d^2 + g_t^2 d_t^2] \right), \end{aligned} \quad (5)$$

$f_{t1}$  is the trip function,  $d_t$  is the distance from the field point to the trip, which is on a wall. The parameter  $\omega_t$  is the wall vorticity at the trip, and  $\Delta U$  is the difference between the velocity at the field point and the trip. The parameter  $g_t \equiv \min(0.1, \Delta U / \omega_t \Delta x)$  where  $\Delta x$  is the grid spacing along the wall at the trip. The constants are

$$\begin{aligned} \sigma = 2/3, \quad c_{b1} = 0.1355, \quad c_{b2} = 0.622, \quad \kappa = 0.41, \\ c_{w1} = c_{b1}/\kappa^2 + (1 + c_{b2})/\sigma, \quad c_{w2} = 0.3, \quad c_{w3} = 2, \quad c_{v1} = 7.1, \\ c_{t1} = 1.0, \quad c_{t2} = 2.0, \quad c_{t3} = 1.1 (1.2), \quad c_{t4} = 2.0 (0.5). \end{aligned} \quad (6)$$

where  $c_{t3}$  and  $c_{t4}$  have two different sets with the values in the brackets considered safer

at high Reynolds numbers [2]. The wall boundary condition is  $\tilde{\nu} = 0$ . In the freestream  $\tilde{\nu} \leq 0.1\nu$  is acceptable.

The S-A model includes the treatment of transition, however, in this study only fully turbulent flow is considered. So with all the transition terms ignored, the transport equation of the S-A model Eqn. (3) can be written as

$$\frac{D\tilde{\nu}}{Dt} = c_{b1}\tilde{\Omega}\tilde{\nu} + \frac{1}{\sigma} [\nabla \cdot ((\nu + \tilde{\nu}) \nabla \tilde{\nu}) + c_{b2} (\nabla \tilde{\nu})^2] - c_{w1}f_w \left[ \frac{\tilde{\nu}}{d} \right]^2. \quad (7)$$

## 2.2 Non-dimensionalisation

The fully turbulent transport equation of the S-A model Eqn. (7) is non-dimensionalised using the freestream flow variables.

$$\begin{aligned} x^* &= \frac{x}{L} & y^* &= \frac{y}{L} & z^* &= \frac{z}{L} \\ u^* &= \frac{u}{U_\infty} & v^* &= \frac{v}{U_\infty} & w^* &= \frac{w}{U_\infty} \\ \rho^* &= \frac{\rho}{\rho_\infty} & \mu^* &= \frac{\mu}{\mu_\infty} & \mu_t^* &= \frac{\mu_t}{\mu_\infty} \\ p^* &= \frac{p}{\rho_\infty U_\infty^2} & T^* &= \frac{T}{T_\infty} & E^* &= \frac{E}{\rho_\infty U_\infty^2} \\ t^* &= \frac{t}{L/U_\infty} & \tilde{\nu}^* &= \frac{\tilde{\nu}}{\nu_\infty} \end{aligned} \quad (8)$$

Variables with superscript notation '\*' are local dimensionless flow variables, freestream variables are variables with subscript notation ' $\infty$ ', and  $L$  is the reference length. The freestream Reynolds number is defined as

$$Re_\infty = \frac{\rho_\infty U_\infty L}{\mu_\infty}. \quad (9)$$

Now the non-dimensional transport equation of the S-A model is written as

$$\frac{D\tilde{\nu}^*}{Dt^*} = c_{b1}\tilde{\Omega}^*\tilde{\nu}^* + \frac{1}{\sigma Re_\infty} [\nabla \cdot ((\nu^* + \tilde{\nu}^*) \nabla \tilde{\nu}^*) + c_{b2} (\nabla \tilde{\nu}^*)^2] - \frac{c_{w1}f_w}{Re_\infty} \left[ \frac{\tilde{\nu}^*}{d^*} \right]^2. \quad (10)$$

For convenience, the superscript '\*' will be dropped so that all the variables are

assumed to be non-dimensional values, unless stated otherwise. For the same purpose, the freestream Reynolds number based on the reference length  $L$  will be written as  $Re$ . Finally the transport equation is written in a similar way as the N-S equations.

$$\frac{\partial W}{\partial t} + \frac{\partial(F^i - F^v)}{\partial x} + \frac{\partial(G^i - G^v)}{\partial y} + \frac{\partial(H^i - H^v)}{\partial z} = S, \quad (11)$$

where  $W = \tilde{v}$ , inviscid flux, viscous flux and the source terms are defined as the following

$$\left\{ \begin{array}{l} F^i = u\tilde{v} \\ G^i = v\tilde{v} \\ H^i = w\tilde{v} \\ F^v = \frac{\nu + \tilde{\nu}}{\sigma Re} \frac{\partial \tilde{v}}{\partial x} \\ G^v = \frac{\nu + \tilde{\nu}}{\sigma Re} \frac{\partial \tilde{v}}{\partial y} \\ H^v = \frac{\nu + \tilde{\nu}}{\sigma Re} \frac{\partial \tilde{v}}{\partial z} \\ S = S_1 + S_2 + S_3 + S_4. \end{array} \right. \quad (12)$$

The source term is divided into the following four parts

$$\left\{ \begin{array}{l} S_1 = c_{b1} \tilde{\Omega} \tilde{v} \\ S_2 = \frac{c_{b2}}{\sigma Re} \left[ \left( \frac{\partial \tilde{v}}{\partial x} \right)^2 + \left( \frac{\partial \tilde{v}}{\partial y} \right)^2 + \left( \frac{\partial \tilde{v}}{\partial z} \right)^2 \right] \\ S_3 = -\frac{c_{w1} f_w}{Re} \left[ \frac{\tilde{v}}{d} \right]^2 \\ S_4 = \tilde{v} \left( \frac{\partial u}{\partial x} + \frac{\partial v}{\partial y} + \frac{\partial w}{\partial z} \right). \end{array} \right. \quad (13)$$

All the auxiliary functions are redefined in non-dimensional form as

$$\begin{aligned}
\chi &\equiv \frac{\tilde{\nu}}{\nu}, \quad f_{v1} = \frac{\chi^3}{\chi^3 + c_{v1}^3}, \quad f_{v2} = 1 - \frac{\chi}{1 + \chi f_{v1}} \\
f_w &= g \left[ \frac{1 + c_{w3}^6}{g^6 + c_{w3}^6} \right]^{1/6}, \quad g = r + c_{w2} (r^6 - r), \quad r \equiv \frac{\tilde{\nu}}{\sqrt{S} \kappa^2 d^2} \cdot \frac{1}{Re} \\
\tilde{\Omega} &= \Omega + \frac{\tilde{\nu}}{\kappa^2 d^2} f_{v2} \cdot \frac{1}{Re}, \quad \Omega \equiv \sqrt{2\Omega_{ij}\Omega_{ij}} \\
\sigma &= 2/3, \quad c_{b1} = 0.1355, \quad c_{b2} = 0.622, \quad \kappa = 0.41
\end{aligned} \tag{14}$$

$$c_{v1} = 7.1, \quad c_{w1} = c_{b1}/\kappa^2 + (1 + c_{b2})/\sigma, \quad c_{w2} = 0.3, \quad c_{w3} = 2.$$

### 2.3 Curvilinear coordinates

The governing equations are usually transformed from the physical domain  $(x, y, z, t)$  to computational domain  $(\xi, \eta, \zeta, \tau)$  with the grid spacing in the computational space is uniform and of unit length. This produces a computational region that is a cuboid and has a regular uniform mesh (Fig. (2.1)).

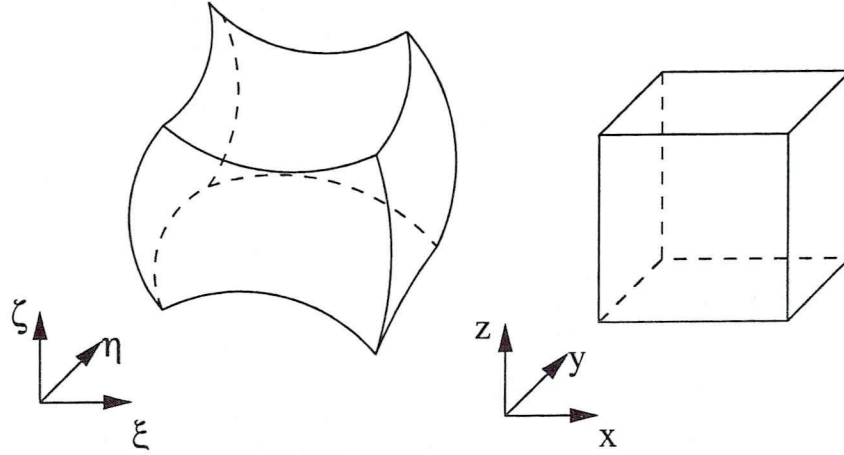


Figure 2.1: *Coordinate transformation from physical to computational domain*

The generalised coordinate transformation produces a system of equations that can be applied to any regular and nonsingular geometry or grid system.

$$\begin{cases} \tau = t \\ \xi = \xi(x, y, z, t) \\ \eta = \eta(x, y, z, t) \\ \zeta = \zeta(x, y, z, t) \end{cases} \quad (15)$$

The Jacobian matrix is defined as

$$\mathbf{J} = \frac{\partial(\xi, \eta, \zeta, \tau)}{\partial(x, y, z, t)} = \begin{bmatrix} \xi_x & \xi_y & \xi_z & \xi_t \\ \eta_x & \eta_y & \eta_z & \eta_t \\ \zeta_x & \zeta_y & \zeta_z & \zeta_t \\ 0 & 0 & 0 & 1 \end{bmatrix}, \quad (16)$$

where

$$\begin{cases} \xi_x = J(y_\eta z_\zeta - y_\zeta z_\eta) & \eta_x = J(z_\xi y_\zeta - y_\xi z_\zeta) & \zeta_x = J(y_\xi z_\eta - z_\xi y_\eta) \\ \xi_y = J(z_\eta x_\zeta - x_\eta z_\zeta) & \eta_y = J(x_\xi z_\zeta - x_\zeta z_\xi) & \zeta_y = J(x_\eta z_\xi - x_\xi z_\eta) \\ \xi_z = J(x_\eta y_\zeta - y_\eta x_\zeta) & \eta_z = J(y_\xi x_\zeta - x_\xi y_\zeta) & \zeta_z = J(x_\xi y_\eta - y_\xi x_\eta) \\ \xi_t = -x_\tau \xi_x - y_\tau \xi_y - z_\tau \xi_z & \eta_t = -x_\tau \eta_x - y_\tau \eta_y - z_\tau \eta_z & \zeta_t = -x_\tau \zeta_x - y_\tau \zeta_y - z_\tau \zeta_z \end{cases} \quad (17)$$

$J$  is the determinant of the Jacobian matrix and can be calculated by

$$J = (x_\xi y_\eta z_\zeta + x_\zeta y_\xi z_\eta + x_\eta y_\zeta z_\xi - x_\xi y_\zeta z_\eta - x_\eta y_\xi z_\zeta - x_\zeta y_\eta z_\xi)^{-1}. \quad (18)$$

All the elements (metrics, e.g.,  $\xi_x, \xi_y, \xi_z$ ) can be obtained from the inverse metrics (e.g.,  $x_\xi, y_\xi, z_\xi$ ). Simple finite difference approximations can be used to calculate these inverse metrics since the grid points are equally spaced in computational space, that is,  $\Delta\xi = \Delta\eta = \Delta\zeta = 1$ .

The chain rule of partial differentiation is introduced in calculating all the derivatives, for example, the velocity gradient  $\frac{\partial u}{\partial x}$  is calculated as

$$\frac{\partial u}{\partial x} = \xi_x \frac{\partial u}{\partial \xi} + \eta_x \frac{\partial u}{\partial \eta} + \zeta_x \frac{\partial u}{\partial \zeta}. \quad (19)$$

Now if we apply the generalised transformation to the transport equation of the S-A turbulence model, Eqn. (11), the following equation will be achieved

$$\frac{\partial \widehat{W}}{\partial \tau} + \frac{\partial (\widehat{F}^i - \widehat{F}^v)}{\partial \xi} + \frac{\partial (\widehat{G}^i - \widehat{G}^v)}{\partial \eta} + \frac{\partial (\widehat{H}^i - \widehat{H}^v)}{\partial \zeta} = \widehat{S}. \quad (20)$$

The variables in the above equation are defined as the following

$$\left\{ \begin{array}{l} \widehat{W} = W/J \\ \widehat{F}^i = \xi_t \widehat{W} + (\xi_x F^i + \xi_y G^i + \xi_z H^i)/J \\ \widehat{G}^i = \eta_t \widehat{W} + (\eta_x F^i + \eta_y G^i + \eta_z H^i)/J \\ \widehat{H}^i = \zeta_t \widehat{W} + (\zeta_x F^i + \zeta_y G^i + \zeta_z H^i)/J \\ \widehat{F}^v = (\xi_x F^v + \xi_y G^v + \xi_z H^v)/J \\ \widehat{G}^v = (\eta_x F^v + \eta_y G^v + \eta_z H^v)/J \\ \widehat{H}^v = (\zeta_x F^v + \zeta_y G^v + \zeta_z H^v)/J \\ \widehat{S} = S/J \end{array} \right. \quad (21)$$

Again derivative terms of the velocity and the working viscosity  $\tilde{\nu}$  should be evaluated in computational space  $(\xi, \eta, \zeta, \tau)$  via the chain rule, as mentioned above.

## 2.4 Finite volume method

The finite volume method uses the integral form of the conservation equation as the starting point

$$\frac{\partial}{\partial t} \int_V \mathbf{W} dV + \int_S (\mathbf{M} \cdot \mathbf{n}) dS = \int_V \mathbf{S}_\phi dV, \quad (22)$$

$$\mathbf{M} = (F^i - F^v)\mathbf{i} + (G^i - G^v)\mathbf{j} + (H^i - H^v)\mathbf{k}. \quad (23)$$

The above integral conservation equation applies to each control volume, as well as

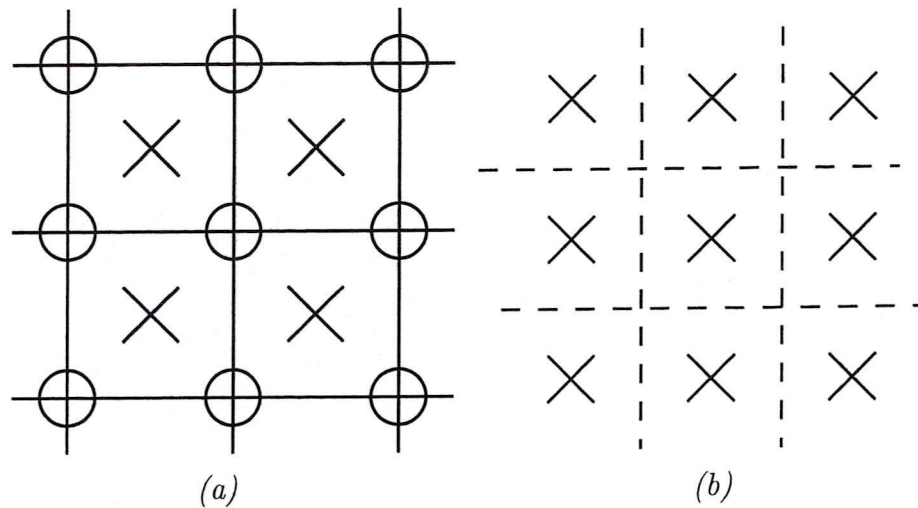


Figure 2.2: *Two types of finite volume grids: (a) nodes centered in CVs (b) CV faces centred between nodes*

to the solution domain as a whole. To obtain an algebraic equation for each control volume, the surface and volume integrals need to be approximated using quadrature formulae.

The usual approach is to define the control volumes by a suitable grid and assign the computational node to the control volume centre. However, it is possible to define the nodal locations first and then construct control volumes around them. Fig. 2.2(a) and Fig. 2.2(b) illustrate these two different finite volume grids. The former one is used in this study.

## 2.5 Spatial discretisation

The application of the finite volume method leads to the need to calculate the fluxes on the surface of two neighbouring control volumes, e.g.,  $\hat{F}_{i\pm 1/2,j,k}^i$ ,  $\hat{F}_{i\pm 1/2,j,k}^v$ . The inviscid flux terms in this study are discretised by the Engquist-Osher method [12]. The MUSCL interpolation [13] is used to provide the third-order accuracy together with van Albada's limiter [14]. The discretisation of the viscous flux terms is realised by central difference. The source term is evaluated at the cell centre.

### 2.5.1 Inviscid flux terms

The Engquist-Osher method is used to discretise the inviscid flux terms:  $\widehat{F}_{i\pm 1/2,j,k}^i$ ,  $\widehat{G}_{i,j\pm 1/2,k}^i$  and  $\widehat{H}_{i,j,k\pm 1/2}^i$ . To describe the method, the flux term  $\widehat{F}_{i+1/2,j,k}^i$  can be written as

$$\widehat{F}_{i+1/2,j,k}^i = \frac{1}{2} \left( \widehat{F}_{i,j,k}^i + \widehat{F}_{i+1,j,k}^i \right) + \frac{1}{2} \int_{\widehat{W}_{i+1/2,j,k}^-}^{\widehat{W}_{i+1/2,j,k}^+} |A(\widehat{W})| d\widehat{W}, \quad (24)$$

where  $A(\widehat{W})$  is the derivative of  $\widehat{F}(\widehat{W})$  with respect to  $\widehat{W}$ . Values for  $\widehat{W}_{i+1/2,j,k}^\pm$  can be obtained from the MUSCL interpolation with von Albada's limiter in order to improve the accuracy of the results.

$$\begin{cases} \widehat{W}_{i+1/2,j,k}^- = \widehat{W}_{i,j,k} + \left[ \frac{(\Delta_+^2 + \epsilon^2)\Delta_- + (\Delta_-^2 + \epsilon^2)\Delta_+}{\Delta_-^2 + \Delta_+^2 + 2\epsilon^2} \right]_{i,j,k} \\ \widehat{W}_{i+1/2,j,k}^+ = \widehat{W}_{i+1,j,k} - \left[ \frac{(\Delta_+^2 + \epsilon^2)\Delta_- + (\Delta_-^2 + \epsilon^2)\Delta_+}{\Delta_-^2 + \Delta_+^2 + 2\epsilon^2} \right]_{i+1,j,k} \end{cases} \quad (25)$$

where

$$\begin{cases} (\Delta_-)_{i,j,k} \equiv \widehat{W}_{i,j,k} - \widehat{W}_{i-1,j,k} \\ (\Delta_+)_{i,j,k} \equiv \widehat{W}_{i+1,j,k} - \widehat{W}_{i,j,k} \end{cases} \quad (26)$$

and  $\epsilon^2$  is a small non-zero constant which can prevent the undesirable clipping of a smooth extremum but otherwise has negligible influence. The value used by van Albada [14] is 0.008. It was found that the results are not very sensitive to the precise value of  $\epsilon^2$ .

According to Eqn. (25), the inviscid flux residual for control volume  $(i, j, k)$  is a function of 13 points

$$R_{i,j,k}^i = R \left( \widehat{W}_{i-2,j,k}, \widehat{W}_{i-1,j,k}, \widehat{W}_{i,j,k}, \widehat{W}_{i+1,j,k}, \widehat{W}_{i+2,j,k}, \widehat{W}_{i,j-2,k}, \right. \\ \left. \widehat{W}_{i,j-1,k}, \widehat{W}_{i,j+1,k}, \widehat{W}_{i,j+2,k}, \widehat{W}_{i,j,k-2}, \widehat{W}_{i,j,k-1}, \widehat{W}_{i,j,k+1}, \widehat{W}_{i,j,k+2} \right). \quad (27)$$

### 2.5.2 Viscous flux terms

Central differencing is used to discretise the viscous flux terms:  $\widehat{F}_{i\pm 1/2,j,k}^v$ ,  $\widehat{G}_{i,j\pm 1/2,k}^v$  and  $\widehat{H}_{i,j,k\pm 1/2}^v$ . The value of the velocity components and their derivatives, as well as the value and derivative of the working eddy viscosity  $\tilde{\nu}$  are required at the faces of each control volume. Control volume face values are approximated by the average of the two adjacent control volume face values,

$$\tilde{\nu}_{i+1/2,j,k} = \frac{1}{2} (\tilde{\nu}_{i,j,k} + \tilde{\nu}_{i+1,j,k}). \quad (28)$$

Control volume face values of the derivatives are obtained using Green's formula applied to a one-sided auxiliary control volume surrounding the considered face, for example

$$\frac{\partial \tilde{\nu}}{\partial x} = \frac{1}{V_{aux}} \iint_{S_{aux}} \tilde{\nu} \, dydz, \quad (29)$$

where  $V_{aux}$  is the volume of the auxiliary control volume and  $S_{aux}$  includes all the six surfaces surrounding the auxiliary control volume. Suppose the centre of the auxiliary control volume is called  $p$ , so the following six values are needed

$$\left\{ \begin{array}{l} \tilde{\nu}_b = (\tilde{\nu}_{i,j,k-1} + \tilde{\nu}_{i+1,j,k-1} + \tilde{\nu}_{i+1,j,k} + \tilde{\nu}_{i,j,k})/4 \\ \tilde{\nu}_w = \tilde{\nu}_{i,j,k} \\ \tilde{\nu}_s = (\tilde{\nu}_{i,j-1,k} + \tilde{\nu}_{i+1,j-1,k} + \tilde{\nu}_{i+1,j,k} + \tilde{\nu}_{i,j,k})/4 \\ \tilde{\nu}_n = (\tilde{\nu}_{i,j,k} + \tilde{\nu}_{i+1,j,k} + \tilde{\nu}_{i+1,j+1,k} + \tilde{\nu}_{i,j+1,k})/4 \\ \tilde{\nu}_e = \tilde{\nu}_{i+1,j,k} \\ \tilde{\nu}_t = (\tilde{\nu}_{i,j,k} + \tilde{\nu}_{i+1,j,k} + \tilde{\nu}_{i+1,j,k+1} + \tilde{\nu}_{i,j,k+1})/4. \end{array} \right. \quad (30)$$

This means that the viscous flux terms are related to 19 points. For both the inviscid and viscous flux terms, the residual is now a function of 25 different points.

### 2.5.3 Source term

The source term is evaluated at the control volume centre, using the approach described in Eqn. (29).

After the spatial discretisation, the following semi-discrete form of the S-A model is achieved

$$\frac{d\widehat{\mathbf{W}}_{i,j,k}}{d\tau} = -\frac{1}{V_{i,j,k}} \mathbf{R}_{i,j,k} \quad (31)$$

where  $\mathbf{R}_{i,j,k}$  denotes the discretisation of the spatial and source terms. Considering the whole computational domain, this equation is rewritten in the following form for clarity

$$\frac{d\mathbf{Q}}{dt} = -\frac{1}{V} \mathbf{R}. \quad (32)$$

## 2.6 Boundary conditions

The boundary conditions are set by using two rows of halo control volumes. Values are set in the halo according to interior values and boundary values. Once halo values are set then all interior control volumes are treated in an identical fashion. The extrapolations used are shown in Table (1). The subscripts 1, 2, b1 and b2 denote values in the interior control volume adjacent to the boundary, the next interior control volume, the first halo control volume and the second halo control volume, respectively.

$\tilde{\nu}_\infty$  is freestream value and is set to  $0.1\nu_\infty$  by default as suggest by Spalart [1]. This value is also used to initialised the flow field. For a given profile bounday,  $\tilde{\nu}_{pro}$  is the value given directly which is set from an input parameter file.

Boundary type	First halo control volume	Second halo control volume
Solid wall	$\tilde{v}_{b1} = -\tilde{v}_2$	$\tilde{v}_{b2} = -\tilde{v}_1$
Far field	$\tilde{v}_{b1} = \tilde{v}_\infty$	$\tilde{v}_{b2} = \tilde{v}_\infty$
y-symmetry	$\tilde{v}_{b1} = \tilde{v}_2$	$\tilde{v}_{b2} = \tilde{v}_1$
z-symmetry	$\tilde{v}_{b1} = \tilde{v}_2$	$\tilde{v}_{b2} = \tilde{v}_1$
Linear extrapolation	$\tilde{v}_{b1} = 2\tilde{v}_{b2} - \tilde{v}_1$	$\tilde{v}_{b2} = 2\tilde{v}_1 - \tilde{v}_2$
Poiseille	$\tilde{v}_{b1} = 0$	$\tilde{v}_{b2} = 0$
Mirror	$\tilde{v}_{b1} = \tilde{v}_1$	$\tilde{v}_{b2} = \tilde{v}_1$
Given profile	$\tilde{v}_{b1} = \tilde{v}_{pro}$	$\tilde{v}_{b2} = \tilde{v}_{pro}$
Degenerated x-y	$\tilde{v}_{b1} = \tilde{v}_2$	$\tilde{v}_{b2} = \tilde{v}_1$
Degenerated x	$\tilde{v}_{b1} = \tilde{v}_2$	$\tilde{v}_{b2} = \tilde{v}_1$
Degenerated interior	$\tilde{v}_{b1} = \tilde{v}_2$	$\tilde{v}_{b2} = \tilde{v}_2$

Table 1: Boundary conditions for the S-A turbulence model

## 2.7 Time discretisation

### 2.7.1 Steady-state solver

The integration in time of Eqn. (32) to a steady-state solution is performed in two phases. First, an explicit scheme is used to smooth out the freestream starting solution.

$$\Delta \mathbf{Q} = -\frac{1}{V} \Delta t \mathbf{R}^n, \quad (33)$$

where  $\Delta \mathbf{Q} = \mathbf{Q}^{n+1} - \mathbf{Q}^n$ ,  $n$  is the current time level,  $n + 1$  is the new time level.

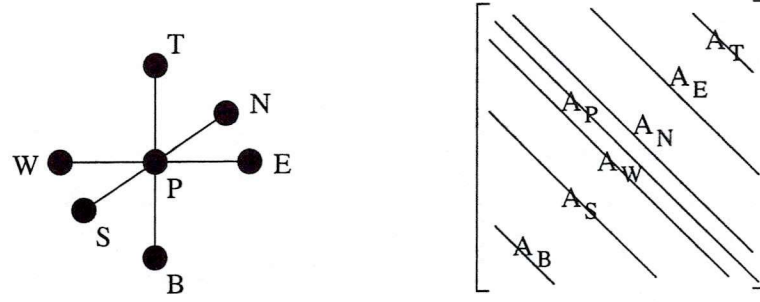
In order to speed up the calculation, an implicit time-marching scheme is applied

$$\frac{V}{\Delta t} \Delta \mathbf{Q} = -\mathbf{R}^{n+1}. \quad (34)$$

This equation represents a system of non-linear algebraic equations. In order to simplify the solution procedure, the flux residual  $\mathbf{R}^{n+1}$  is linearised in time as follows

$$\begin{aligned} \mathbf{R}^{n+1} &= \mathbf{R}^n + \frac{\partial \mathbf{R}}{\partial t} \Delta t + O(\Delta t^2) \\ &\approx \mathbf{R}^n + \frac{\partial \mathbf{R}}{\partial \mathbf{Q}} \frac{\partial \mathbf{Q}}{\partial t} \Delta t \\ &\approx \mathbf{R}^n + \frac{\partial \mathbf{R}}{\partial \mathbf{Q}} \Delta \mathbf{Q}. \end{aligned} \quad (35)$$

Now the following linear system is obtained after applying the above approximation

Figure 2.3: *Approximate Jacobian matrix*

$$\left( \frac{V}{\Delta t} \mathbf{I} + \frac{\partial \mathbf{R}}{\partial \mathbf{Q}} \right) \Delta \mathbf{Q} = -\mathbf{R}^n. \quad (36)$$

As mentioned above, the residual of each control volume is related to 25 points. This leads to a Jacobian matrix  $\partial \mathbf{R} / \partial \mathbf{Q}$  which has twenty five non-zero blocks per row. An approximate Jacobian is introduced in order to reduce the memory requirement and CPU time consumption. Only seven non-zero elements are considered so that when calculating the Jacobian the residual is only considered to be a function of these seven points

$$R_{i,j,k} = R(Q_{i-1,j,k}, Q_{i,j,k}, Q_{i+1,j,k}, Q_{i,j-1,k}, Q_{i,j+1,k}, Q_{i,j,k-1}, Q_{i,j,k+1}). \quad (37)$$

This approximation, as shown in Fig. (2.3), which is applied only for the derivation of the Jacobian terms, is also easier for the linear solver because the resulting matrix becomes more diagonally dominant than using the exact Jacobians. As a result, 72% of the memory requirement and matrix-vector multiplication operation are reduced. The method has been successfully applied in the two-dimensional solver PMB2D [15] and the mean flow solver of the PMB3D code.

### 2.7.2 Unsteady flow solver

The N-S equations and the S-A transport equation for unsteady flow are solved by introducing an iteration through pseudo time  $\tau$  to the steady state [16], as given by

$$\frac{\mathbf{w}^{n+1,m+1} - \mathbf{w}^{n+1,m}}{\Delta\tau} + \frac{3\mathbf{w}^{k_m} - 4\mathbf{w}^n + \mathbf{w}^{n-1}}{2\Delta t} + \mathbf{R}(\tilde{\mathbf{w}}^{k_m}, \tilde{\mathbf{q}}^{k_t}) = 0 \quad (38)$$

$$\frac{\mathbf{q}^{n+1,m+1} - \mathbf{q}^{n+1,m}}{\Delta\tau} + \frac{3\mathbf{q}^{l_t} - 4\mathbf{q}^n + \mathbf{q}^{n-1}}{2\Delta t} + \mathbf{S}(\tilde{\mathbf{w}}^{l_m}, \tilde{\mathbf{q}}^{l_t}) = 0, \quad (39)$$

where the  $m$ -th pseudo time iterate at the  $(n+1)$ th real time step are denoted by  $\mathbf{w}^{n+1,m}$  and  $\mathbf{q}^{n+1,m}$  respectively. Here  $k_m, k_t, l_m$  and  $l_t$  give the time level of the variables used in the spatial discretisation. The iteration scheme used only effects the efficiency of the method and hence we can sequence the solution in pseudo time without compromising accuracy. For example, using explicit time stepping we can calculate  $\mathbf{w}^{n+1,m+1}$  using  $k_m = n+1, m$  and  $k_t = n+1, m$  and  $\mathbf{q}^{n+1,m+1}$  using  $l_m = n+1, m+1$  and  $l_t = n+1, m$ . For implicit time stepping in pseudo time  $k_m = l_m = l_t = n+1, m+1$  and  $k_t = n+1, m$  can be used. In both of these cases the solution of the equations is decoupled by freezing values but at convergence the real time stepping proceeds with no sequencing error. It is easy to recover a solution which is sequenced in real time from this formulation by setting  $k_t = n, m$  throughout the calculation of the pseudo steady state. This facilitates a comparison of the current pseudo time sequencing with the more common real time sequencing.

## 2.8 Linear solver

For the implicit scheme, the result of the discretisation process is a system of algebraic equations, Eqn. (36) is written here again.

$$\left( \frac{V}{\Delta t} \mathbf{I} + \frac{\partial \mathbf{R}}{\partial \mathbf{Q}} \right) \Delta \mathbf{Q} = -\mathbf{R}^n. \quad (40)$$

For unsteady problems, the equation should be changed because of the additional term in Eqn. (39).

The generalised conjugate gradient (GCG) method [17] with the block incomplete LU (BILU) decomposition [18] are chosen to be used to solve this system.

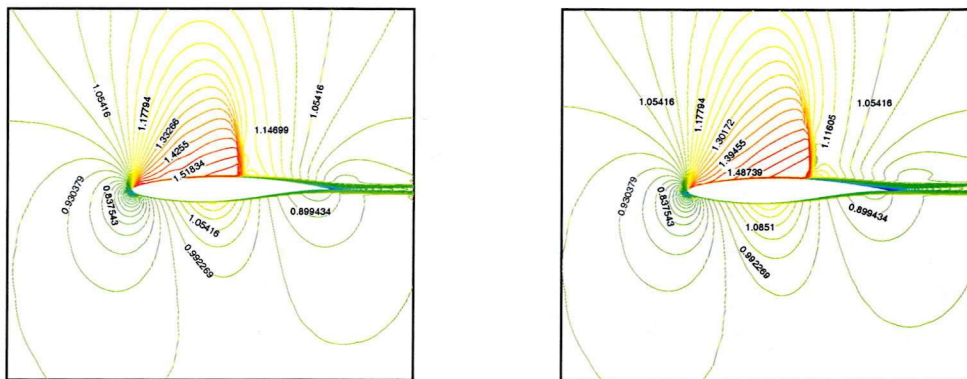
### 3 Validation

#### 3.1 RAE2822 aerofoil Cases 9 and 10

The transonic flow over an aerofoil provides a good test of the turbulence model to predict the boundary layer development along a curved surface. Two cases of RAE2822, Case 9 (no/small separation region) and Case 10 (shock induced separation) with different flow conditions were tested. Flow conditions for these two cases are listed in Table 2. For both cases, the same C-type grid was generated with 257 points in the streamwise direction, 65 points in the direction normal to the wall and 5 points in the spanwise direction. Since the transitional terms of the S-A turbulence model was ignored in the implementation, flow around this aerofoil was considered fully turbulent.

RAE2822	$M_\infty$	$Re$	Angle of attack	Transition at $x/c$
Case 9	0.73	$6.5 \times 10^6$	$2.79^\circ$	0.03
Case 10	0.75	$6.2 \times 10^6$	$2.81^\circ$	0.03

Table 2: Flow conditions selected for the RAE2822 Cases 9 and 10



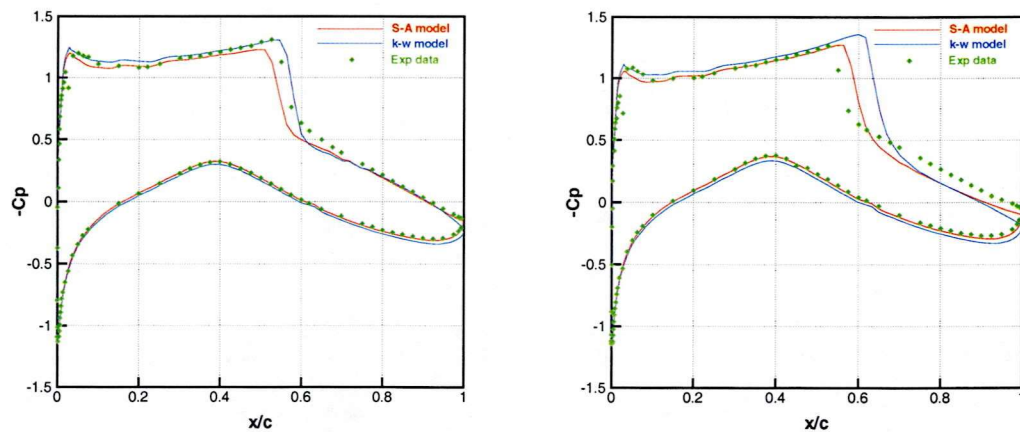
(a) RAE2822 Case 9

(b) RAE2822 Case 10

Figure 3.1: Mach number contours around the RAE2822 aerofoil

Mach contours, pressure and skin friction coefficient distributions for both cases compared with the  $k - \omega$  turbulence model and the experimental data are presented in

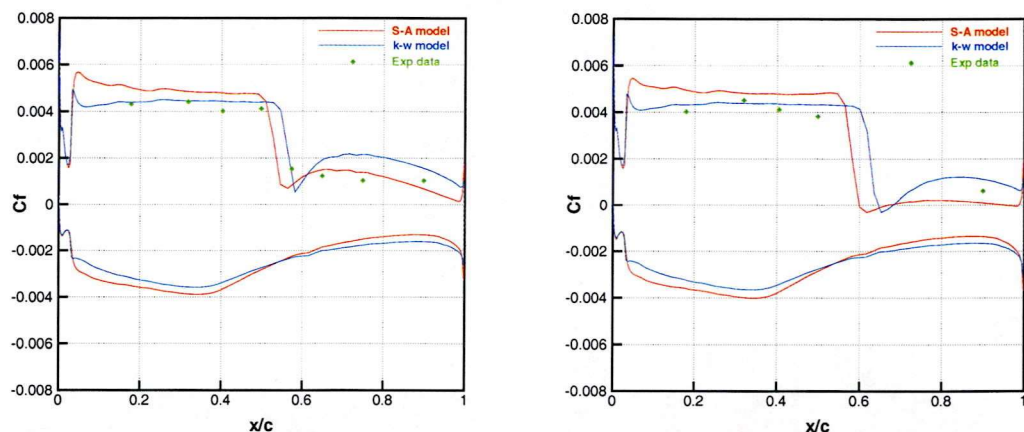
Figs. 3.1, 3.2 and 3.3. Shock was captured in both cases. For Case 9, the location of the shock captured is upstream from the experimental location. For Case 10, the the shock captured is downstream from the experimental data. The  $k - \omega$  model gives the shock location downstream of the experimental data in both cases. The angle of attack has a strong influence on the shock location. Since the correct angle of attack is uncertain, the shock location is not a reliable indicator of the turbulence model accuracy in these two cases.



(a) RAE2822 Case 9

(b) RAE2822 Case 10

Figure 3.2: Pressure coefficient distributions for the RAE2822 aerofoil



(a) RAE2822 Case 9

(b) RAE2822 Case 10

Figure 3.3: Skin friction coefficient distributions for the RAE2822 aerofoil

In Fig. 3.2, pressure coefficient distributions on lower wall surface are quite good in both cases for both turbulence models. But on the upper wall surface, shock position is not well predicted as mentioned above. Shock induced separation can be observed in Case 10 (Fig. 3.3).

### 3.2 NLR-F5 wing

A second test was made to investigate the flow around a NLR-F5 wing. The flow conditions are as follows: the freestream Mach number is 0.896, the attack angle is  $0.497^\circ$  and the Reynolds number is  $5.79 \times 10^6$ . A C-O type grid which containing  $65 \times 33 \times 33$  points was used in this calculation.

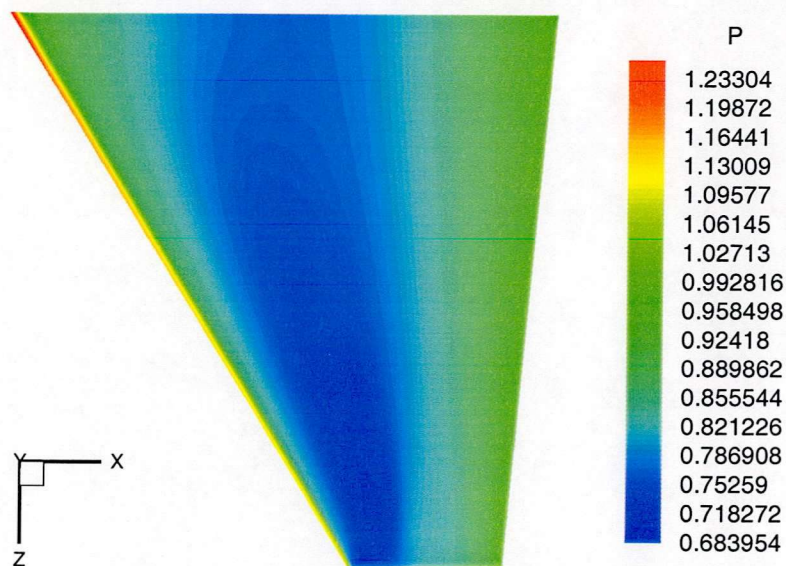


Figure 3.4: *Pressure contours for NLR-F5 wing*

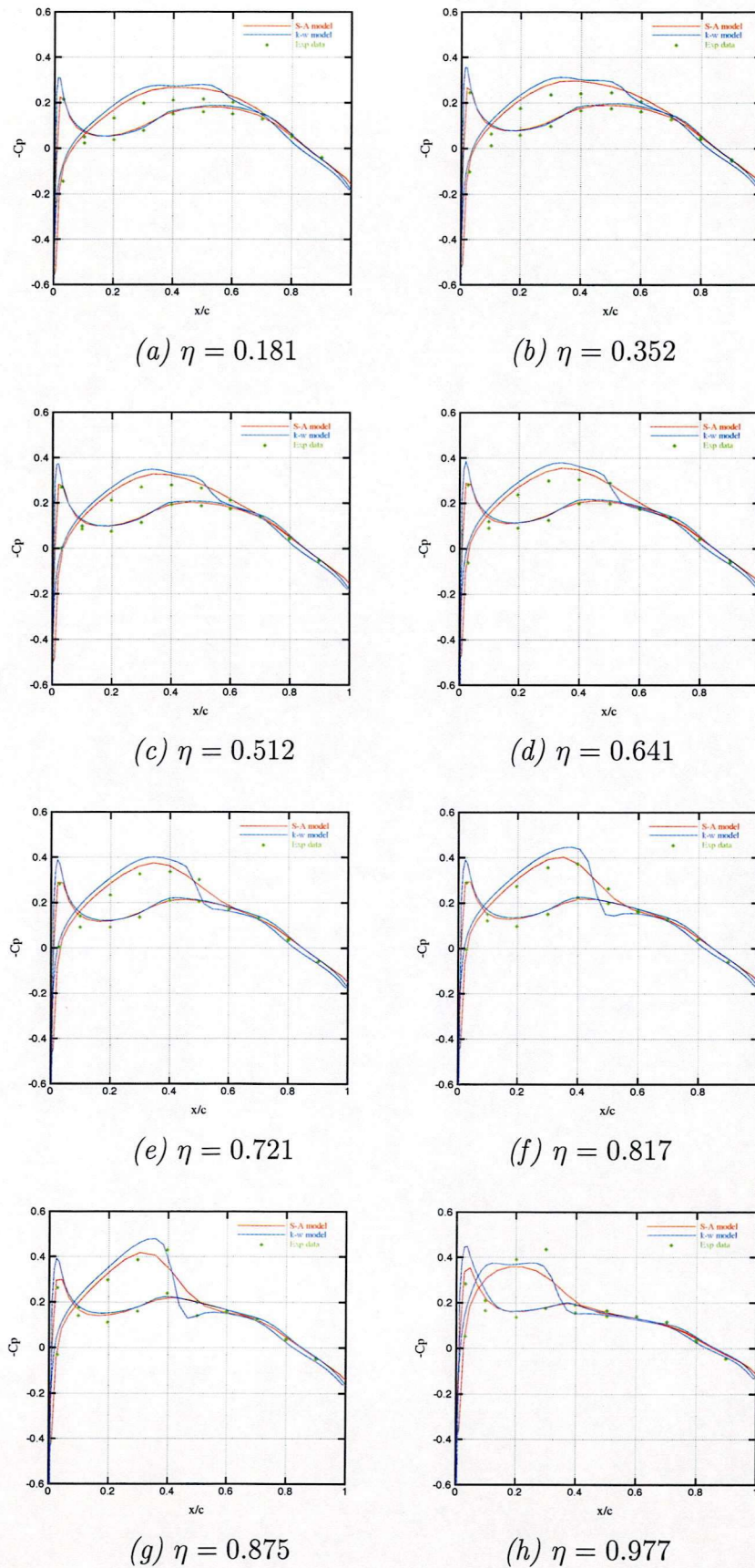


Figure 3.5: Pressure coefficient distribution for NLR-F5 Wing

Pressure contour is shown in Fig. 3.4 with the shock near the leading edge clearly seen. In Fig. 3.5, the pressure coefficient distributions are compared with the  $k - \omega$  model and the experimental data.  $\eta$  means the position along spanwise direction. In the region near the lower surface leading-edge, the S-A model predicts the suction peak very well. In the area near the tip (Fig. 3.5 (g)  $\eta = 0.875$  and (h)  $\eta = 0.977$ ) the S-A model does not capture the shock wave on the upper wall surface, while the  $k - \omega$  model predicts the shock sharply.

### 3.3 ONERA A aerofoil

The ONERA A aerofoil at a freestream Mach number  $M_\infty = 0.15$ , Reynolds number  $Re = 2 \times 10^6$  and an angle of attack  $\alpha = 13.3^\circ$  has been considered as a validation case for the S-A turbulence model.

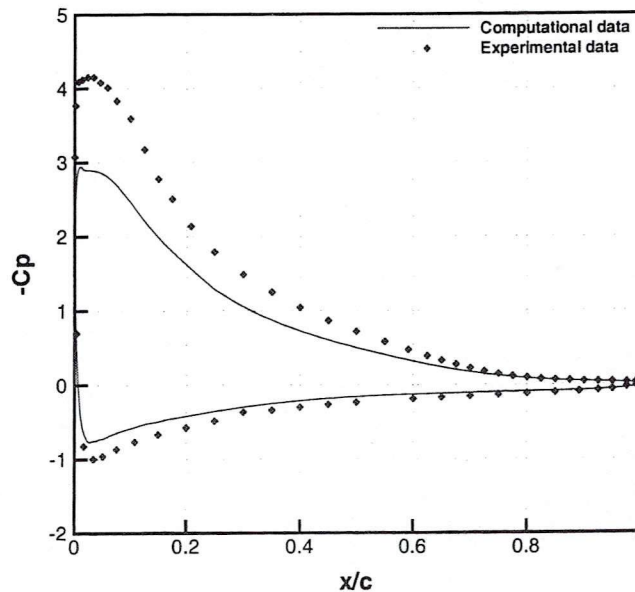


Figure 3.6: *Pressure coefficient distribution along the ONERA A aerofoil*

Because of the high attack angle, boundary layer separation on the upper surface near the trailing edge is a challenging test case for turbulence models. Both the separation point and the recirculation structure should be correctly predicted in order to

obtain the correct lift coefficient and overall pressure distribution on the aerofoil. A C-type mesh was used with  $6 \text{ blocks containing } 341 \times 45 \times 2$  grid points.

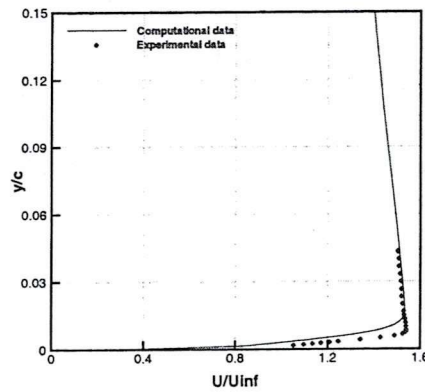
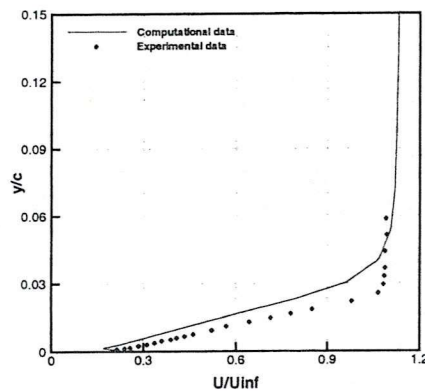
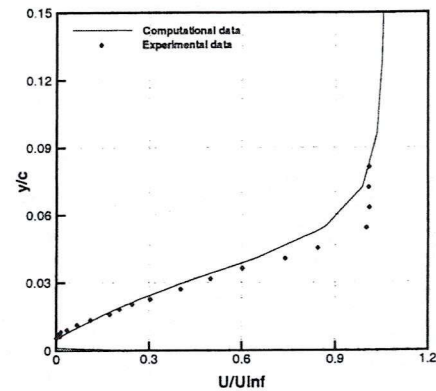
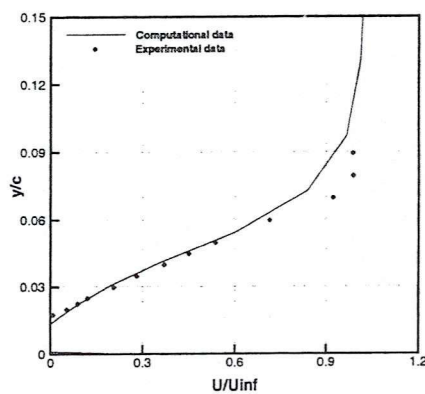
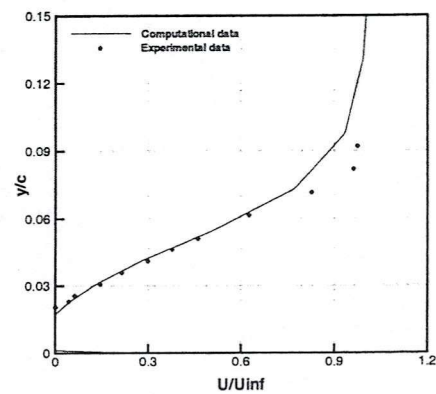
(a)  $x/c = 0.3$ (b)  $x/c = 0.7$ (c)  $x/c = 0.87$ (d)  $x/c = 0.96$ (e)  $x/c = 0.99$ 

Figure 3.7: Velocity profiles along the ONERA A aerofoil

Pressure coefficient obtained from the present model is compared with the exper-

imental data in Fig. 3.3. In the near leading edge region, a big difference is observed due to lack of transition and the large attack angle. In the area near the trailing edge, this model gives much closer results.

Velocity profiles at five positions along the aerofoil are compared with experimental results in Fig. 3.3. In general, the agreement is fairly good at the outer part of the boundary layer. Boundary layer separation on the upper surface near the trailing edge is observed in Fig. 3.3 (d), (e) and (f).

### 3.4 AGARD Case CT2

For the AGARD Case CT2, the NACA0012 aerofoil rotates around the moment centre, one quarter of the chord. The incidence is given by the following equation.

$$\alpha(t) = 3.16^\circ + 4.59^\circ \sin(\omega t) \quad (41)$$

where  $\omega = k/2$  is the angular frequency of the motion ( $k = 0.0811$ ). There are  $129 \times 33 \times 2$  grid points in the computational domain and the grids are rotating rigidly with the aerofoil. The freestream Mach number is 0.6 and the Reynolds number is 4.8 million. The mesh used in this calculation was a H-type mesh with  $149 \times 65$  grid points on two blocks located upper and lower of the aerofoil. Another four blocks were also included with  $65 \times 25$  grid points in each block.

In Fig. 3.8, normal force comparison shows good agreement between the computation and experiment. Pressure distributions are compared at four angles of incidence in Fig. 3.9. It is observed that a shock wave occurs when the attack angle is near the maximum value but the shock wave strength is under-estimated.

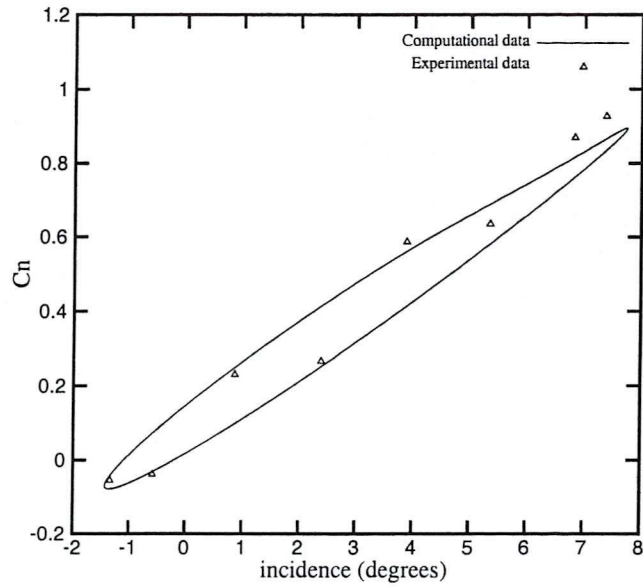
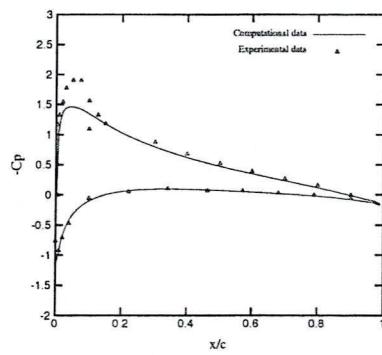
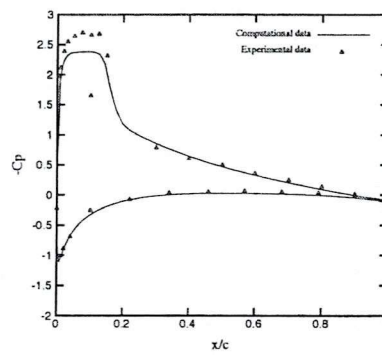


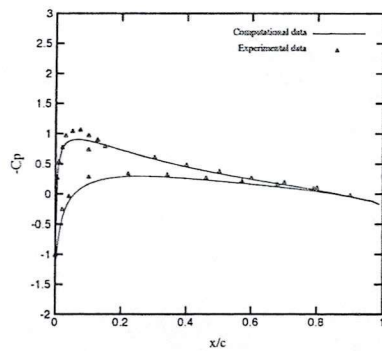
Figure 3.8: *Integrated normal force for NACA0012 aerofoil case CT2*



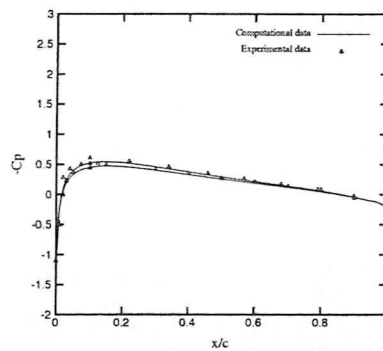
(a)  $\alpha = 5.32^\circ$  up



(b)  $\alpha = 6.80^\circ$  down



(a)  $\alpha = 0.86^\circ$  down

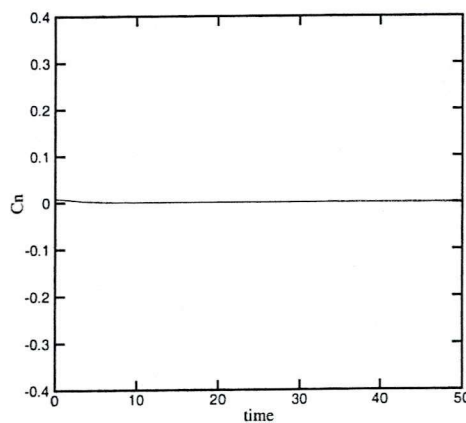


(b)  $\alpha = -1.30^\circ$  down

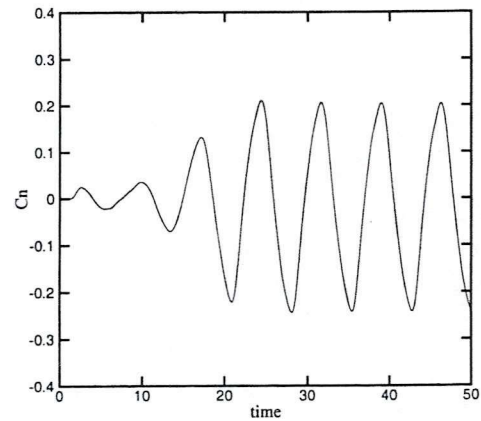
Figure 3.9: *Instantaneous pressure distributions for NACA0012 aerofoil case CT2*

### 3.5 Self excited test case

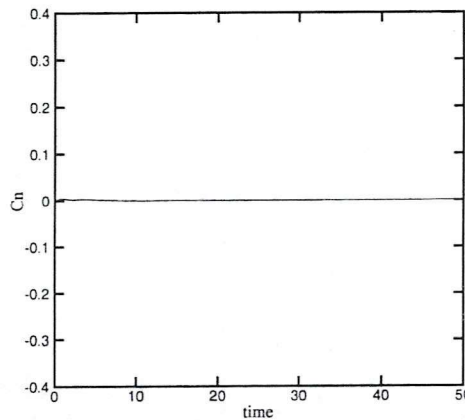
For flow over an 18% circular arc aerofoil, experimental studies have found that the flow depends on the flow conditions and history. Three distinct regions have been observed: (1) Below a critical Mach number the flow is steady with trailing edge separation. (2) For larger Mach numbers shock induced separation is observed and the flow becomes unsteady. (3) The flow becomes steady again as the Mach number is increased. In this case, the Reynolds number is 2 million, when the Mach number is between 0.7 and 0.8, unsteady flow is observed. While the Mach number is below 0.7 or over 0.8, steady flow is observed in the experimental studies.



(a)  $M_\infty = 0.68$ ,  $Re = 2 \times 10^6$



(b)  $M_\infty = 0.77$ ,  $Re = 2 \times 10^6$



(c)  $M_\infty = 0.82$ ,  $Re = 2 \times 10^6$

Figure 3.10: Normal force coefficient history for 18% circular arc aerofoil test case

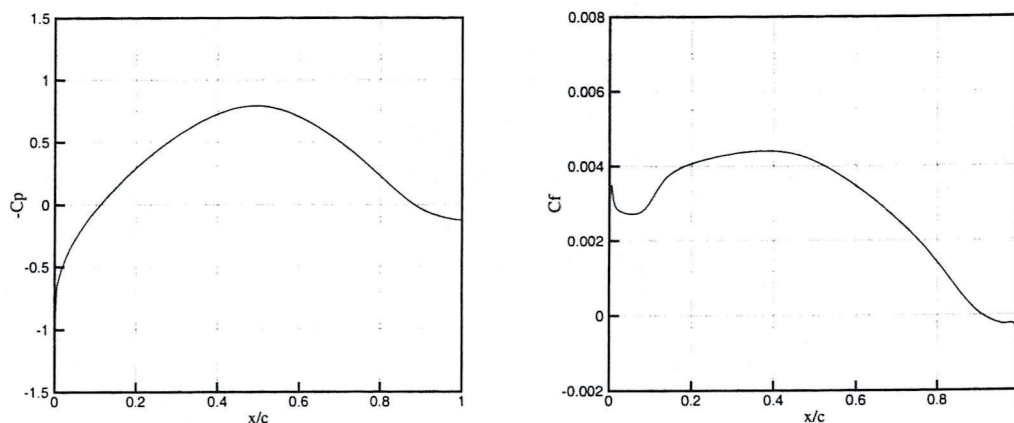
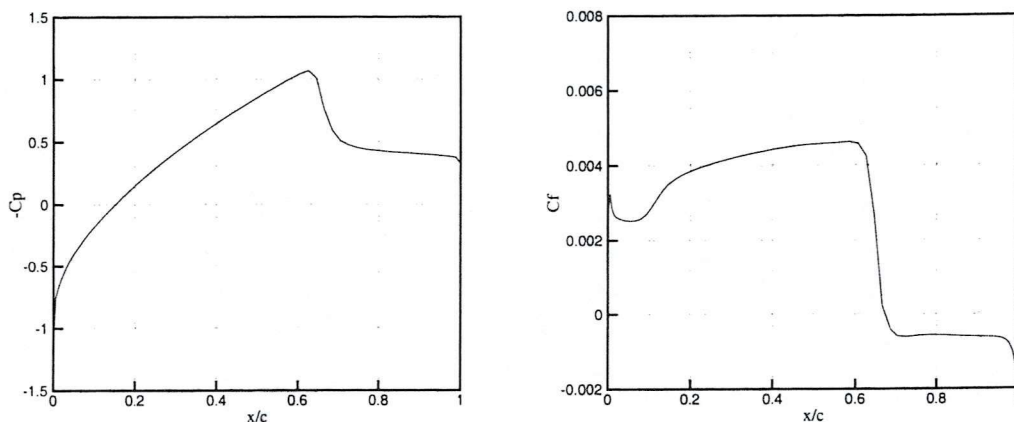
(a)  $M_\infty = 0.68$ ,  $Re = 2 \times 10^6$ (b)  $M_\infty = 0.82$ ,  $Re = 2 \times 10^6$ 

Figure 3.11: Steady pressure and skin friction distributions for 18% circular arc aerofoil test case CT2

The grids used here include  $123 \times 33 \times 2$  grid points. From the normal force history for three different Mach numbers (0.68, 0.77 and 0.82) in Fig. 3.10, it is clear that the computation successfully reproduced all these three flow types observed in the experiments. Pressure and skin friction distributions of the two steady cases at Mach number of 0.68 and 0.82 are presented in Fig. 3.11, for the high Mach number case shock induced separation is clearly observed. For the unsteady case, the shock wave moves forward, then backward with flow separation as shown in Fig. 3.12.

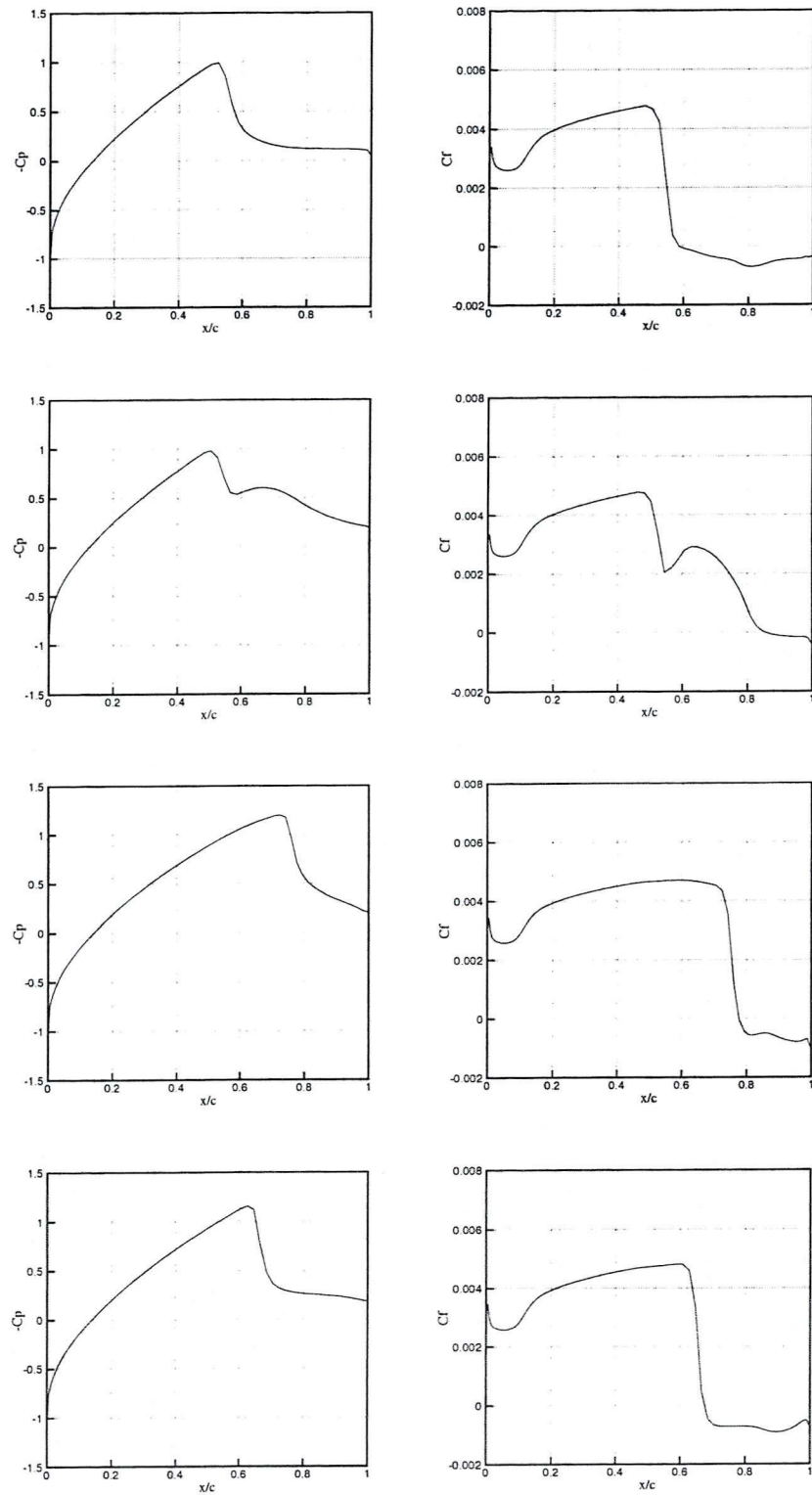


Figure 3.12: Unsteady pressure and skin friction distribution sequence for 18% circular arc aerofoil test case,  $M_\infty = 0.77$ ,  $Re = 2 \times 10^6$

## 4 Conclusions

The implementation of the Spalart-Allmaras turbulence model in the PMB3D code gives some reasonable results in the validation phase. For all the test cases including RAE2822 aerofoil Cases 9 and 10, NLR-F5 wing, ONERA A aerofoil, AGARD Case CT2 and an 18% circular arc aerofoil, the S-A model captured all the main flow phenomena both in steady and unsteady problem. It seems that this model is promising especially for flows without considerable separation.

## References

- [1] P.R. Spalart and S.R. Allmaras. A one-equation turbulence model for aerodynamic flows. *AIAA Paper 92-0439*, 1992.
- [2] P.R. Spalart and S.R. Allmaras. A one-equation turbulence model for aerodynamic flows. *La Recherche Aéronautique*, 1:5-21, 1994.
- [3] B.S. Baldwin and T.J. Barth. A one-equation turbulence transport model for high Reynolds number wall-bounded flows. *AIAA Paper 91-0610*, 1991.
- [4] J.E. Bardina, P.G. Huang, and T.J. Coakley. Turbulence modeling validation, testing and development. NASA TM-110446, National Aeronautics and Space Administration, April 1997.
- [5] L.D. Kral. Recent experience with different turbulence models applied to the calculation of flow over aircraft components. *Progress in Aerospace Sciences*, 34(7-8):481-541, 1998.
- [6] C.L. Rumsey and V.N. Vatsa. A comparison of the predictive capabilities of several turbulence models using upwind and central-difference computer codes. *AIAA Paper 93-0192*, 1993.
- [7] M. Mani, P. Willhite, and J. Ladd. Performance of one-equation turbulence models in cfd applications. *AIAA Paper 95-2221*, 1995.
- [8] G.R. Srinivasan, J.A. Ekaterinaris, and W.J. McCroskey. Evaluation of turbulence models for unsteady flows of an oscillating airfoil. *Computers & Fluids*, 24(7):833-861, 1995.
- [9] V.A. Sai and F.M. Lutfy. Analysis of the Baldwin-Barth and Spalart-Allmaras one-equation turbulence models. *AIAA Journal*, 33(10):1971-1974, 1995.

- [10] J.R. Edwards and S. Chandra. Comparison of eddy viscosity-transport turbulence models for three-dimensional, shock-separated flowfields. *AIAA Journal*, 34(4):756–763, 1996.
- [11] R. Paciorri, W. Dieudonné, G. Degrez, J.M. Charbonnier, and H. Deconinck. Exploring the validity of the Spalart-Allmaras turbulence model for hypersonic flows. *AIAA Journal*, 35(2):121–126, 1998.
- [12] B. Enquist and S. Osher. One-sided difference approximations for nonlinear conservation laws. *Mathematics of Computation*, 36(154):321–351, 1981.
- [13] B. van Leer. Towards the ultimate conservative difference scheme. V. A second-order sequel to Godunov’s method. *Journal of Computational Physics*, 32:101–136, 1979.
- [14] G.D. van Albada, B. van Leer, and Jr. W.W. Roberts. A comparative study of computational methods in cosmic gas dynamics. *Astronomy and Astrophysics*, 108:76–84, 1982.
- [15] F. Cantariti, L. Dubuc, B. Gribben, M. Woodgate, K. J. Badcock, and B. E. Richards. Approximate Jacobians for the solution of the Euler and Navier-Stokes equations. Technical report, University of Glasgow, UK, 1997.
- [16] K. Badcock, F. Cantariti, and B. Gribben. Theory guide to Pmb2D version 3.0. Technical report, University of Glasgow, UK, July 1998.
- [17] O. Axelsson. *Iterative Solution Methods*. Cambridge University Press, 1994.
- [18] J.H. Ferziger and M. Perić. *Computational Methods for Fluid Dynamics*. Springer, 1997.

